Received: 22 April 2022 | Revised: 15 September 2022 | Accepted: 28 September 2022

DOI: 10.1002/hbm.26125

RESEARCH ARTICLE

WILEY

Comprehensive shape analysis of the cortex in Huntington's disease

Zachary A. Stoebner[1,2] | Kilian Hett[1] | Ilwoo Lyu[1,3] | Hans Johnson[4] | Jane S. Paulsen[5] | Jeffrey D. Long[6,7] | Ipek Oguz[1]

[1]Department of Computer Science, Vanderbilt University, Nashville, Tennessee, USA

[2]University of Texas at Austin, Austin, Texas, USA

[3]Department of Computer Science and Engineering, UNIST, Ulsan, South Korea

[4]Department of Electrical and Computer Engineering, University of Iowa, Iowa City, Iowa, USA

[5]Department of Neurology, University of Wisconsin, Madison, Wisconsin, USA

[6]Department of Psychiatry, University of Iowa, Iowa City, Iowa, USA

[7]Department of Biostatistics, University of Iowa, Iowa City, Iowa, USA

Correspondence
Ipek Oguz, Department of Computer Science, Vanderbilt University, Nashville, Tennessee, USA.
Email: ipek.oguz@vanderbilt.edu

Ilwoo Lyu, Department of Computer Science and Engineering, UNIST, Ulsan, South Korea.
Email: ilwoolyu@unist.ac.kr

Funding information
CHDI Foundation; National Center for Advancing Translational Sciences; National Institutes of Health, Grant/Award Numbers: R01-NS040068, R01-NS094456 U01-NS103475, U01-NS105509; NRF Korea, Grant/Award Number: 2021R1G1A1094359; CHDI Foundation (U.S.), the U.S. National Institutes of Health, Grant/Award Numbers: NS040068, NS119471, NS114065, NS105709, NS049206, NS016367, NS091161, NS082079; Medical Research Council, Grant/Award Numbers: MR/P001629/1, MR/L010305/1

Abstract

The striatum has traditionally been the focus of Huntington's disease research due to the primary insult to this region and its central role in motor symptoms. Beyond the striatum, evidence of cortical alterations caused by Huntington's disease has surfaced. However, findings are not coherent between studies which have used cortical thickness for Huntington's disease since it is the well-established cortical metric of interest in other diseases. In this study, we propose a more comprehensive approach to cortical morphology in Huntington's disease using cortical thickness, sulcal depth, and local gyrification index. Our results show consistency with prior findings in cortical thickness, including its limitations. Our comparison between cortical thickness and local gyrification index underscores the complementary nature of these two measures—cortical thickness detects changes in the sensorimotor and posterior areas while local gyrification index identifies insular differences. Since local gyrification index and cortical thickness measures detect changes in different regions, the two used in tandem could provide a clinically relevant measure of disease progression. Our findings suggest that differences in insular regions may correspond to earlier neurodegeneration and may provide a complementary cortical measure for detection of subtle early cortical changes due to Huntington's disease.

KEYWORDS
cortical analysis, cortical shape, Huntington's disease

Abbreviations: CAG, cytosine-adenosine-guanine; CAP, CAG-Age product; CT, cortical thickness; LGI, local gyrification index; SD, sulcal depth; TICV, total intra-cranial volume.

Clinical investigators contributing to the European Huntington's Disease Network, Huntington Study Group and Enroll-HD studies are listed at links provided in the Acknowledgments.

1 | INTRODUCTION

Huntington's disease is an inherited, progressive, autosomal-dominant neurodegenerative disorder. The typical life expectancy is 20 years from motor diagnosis. Huntington's disease symptoms are characterized by chorea, lack of coordination, dystonia, cognitive decline, and changes in behavior. Usually onset is during middle-age (~30–50 years; Walker, 2007).

HD is caused by an expansion of 36 or more repeats of a cytosine-adenosine-guanine [CAG] trinucleotide in the huntingtin gene. Full penetrance occurs at 41 or more CAG repeats, partial penetrance occurs from 36 to 40 CAG repeats. Intermediate alleles are 26–35 repeats, where mutation can occur across generations. Repeat lengths <26 are considered healthy (Walker, 2007). Age of motor onset has a strong inverse relationship with CAG length. Due to the strong association of gene mutation length and age at Huntington's disease diagnosis, personal onset age can be roughly estimated from the number of trinucleotide repeats multiplied by the current age. Unfortunately, these estimates have large confidence intervals, leading to considerable variability in the CAG strata. Some of this variability can be explained by genetic variants (Long et al., 2018) and imaging, clinical, and demographic variables (Paulsen et al., 2015).

The neurodegeneration caused by Huntington's disease is mainly focal, preferentially targeting striatal medium spiny neurons, which are instrumental to the basal ganglia-thalamocortical circuitry. The indirect pathway of this circuit is crucial to motor control by preventing unwanted muscle contractions and facilitating motor control guided by the cortex (Ehrlich, 2012). Particular regions that substantially atrophy from Huntington's disease are the caudate nucleus and the putamen, the globus pallidum, substantia nigra, parts of the cerebral cortex, hippocampus, cerebellum, hypothalamus, and thalamus (Walker, 2007). While prior Huntington's disease studies have focused on subcortical regions (Hett et al., 2020; Li et al., 2020; Li et al., 2021a; Li et al., 2021b), evidence of cortical changes suggests that there might be an alternative mechanism of neurodegeneration than that which causes subcortical changes (Paulsen et al., 2010; Paulsen et al., 2015). Neurodegeneration in the cerebral cortex has been reported and may be partly responsible for non-choreic symptoms such as dementia, irritability, apathy, and depression, motivating our study of the cortical surface (Hedreen et al., 1991). Our overarching hypothesis is that detecting differences in the broader cortex through complementary measures may be integral to developing better measures of detection and gaining more insight into disease progression towards a better understanding of the complexity of Huntington's disease pathophysiology.

Former studies of the cortical alterations in Huntington's disease have based their analysis on cortical thickness (Nopoulos et al., 2010; Rosas et al., 2002; Tabrizi et al., 2013). However, cortical thickness can be prone to local measurement noise and does not entirely characterize the morphology of the cerebral cortex. For example, the insula was largely undetected by cortical thickness, yet differences in the insula and basal ganglia have been tied to impaired disgust processing in pre-symptomatic Huntington's disease, which might be useful for early detection (Hennenlotter et al., 2004). Hence, in this study we undertake a more thorough study of cortical neurodegeneration in Huntington's disease through a more complete set of descriptors, namely, cortical thickness (Fischl & Dale, 2000), sulcal depth (Lyu, Kang, Woodward, & Landman, 2018), and local gyrification index (Lyu, Kim, Girault, et al., 2018).

The central hypothesis of this study is that a more comprehensive shape analysis on specific cortical features may uncover more Huntington's disease-caused cortical alterations than previously known. Other shape analyses often assess general atrophy, analyzing whole-brain segmentation (Wu et al., 2018), the subcortical structures (Tan et al., 2018; Tang et al., 2019), or the white matter tracts connecting subcortical structures to cortical areas corresponding to certain functions (Hong et al., 2018). In contrast, we focus only on the cortical surface, and we estimate cortical changes using three complementary cortical shape features—cortical thickness, sulcal depth, and local gyrification index—to discover significant differences in affected cortical regions. Our findings identify robust cortical alterations in Huntington's disease that complement striatal atrophy, which has been extensively studied. The results of the endeavor have direct utility for neuroscience by identifying novel markers of neurodegeneration in Huntington's disease, determining areas that differ significantly on the cortical surface of Huntington's disease patients, and contributing to the detection and tracking of Huntington's disease progression.

2 | MATERIALS AND METHODS

2.1 | Demographics

The Huntington's disease dataset analyzed throughout this project was provided by the PREDICT-HD study (Paulsen et al., 2008) which is a multi-site longitudinal study focused on improving the prediction of Huntington's disease diagnosis, identifying its markers of progression, and improving the reliability of measures. For this study, we select the subset of PREDICT-HD that consists of participants who completed at least two sessions using 3 T MRI.

A widely used progression index is the CAG-Age Product, $\mathrm{CAP} = \mathrm{Age}_0 \times (\mathrm{CAG} - 33.66)$, where Age_0 is the age of the subject at the time of first MRI scan and *CAG* is the length of their CAG expansion (Zhang et al., 2011). Following conventional practice, we classify patients with similar severity of pathology into three distinct CAP groups: $\mathrm{CAP}_{\mathrm{low}}$ (CAP < 290), $\mathrm{CAP}_{\mathrm{medium}}$ (290 ≤ CAP < 368), and $\mathrm{CAP}_{\mathrm{high}}$ (CAP ≥ 368; Zhang et al., 2011).

In total, this dataset is composed of 1083 MRIs (see Table 1 for more details). We note that subjects undergo scanning sessions at different time points in their disease progression, which is important to account for in modeling the progression of individual patterns of neurodegeneration.

2.2 | Cortical surface reconstruction and spherical mapping

Skull stripping, tissue segmentation, and surface reconstruction were performed with the FreeSurfer v6.0 pipeline (Fischl, 2012). To

TABLE 1 Demographic description of the analyzed cohort

(a)	Overall	Control	CAP_{low}	CAP_{med}	CAP_{high}
# Sessions	1083	323	261	282	217
# Subjects	395	111	98	103	83
Age (SD)	46.72 (12.61)	49.48 (12.00)	37.76 (9.81)	47.73 (12.15)	52.1 (11.61)
CAG interval	[15,58]	[15, 35]	[37,45]	[38,48]	[39,58]
Gender (F:M)	716: 367	205: 118	186: 75	207: 75	118: 99

standardize the data and reduce bias, the reconstructed surfaces are then spherically deformed via surface registration with minimal distortion (Lyu et al., 2019). Each surface is resampled into the same number of vertices (# = 163,842) via icosahedral subdivision. Only these resampled surfaces are used for statistical shape analysis. Note that surface-related processing used the originally reconstructed surfaces to avoid any potential loss of information from the resampling process. Cortical surface parcellation is independently obtained via a spherical neural network (Parvathaneni et al., 2019) using the BrainCOLOR (Klein et al., 2010) protocol with 49 cortical labels per hemisphere and defines the region boundaries of the reconstruction. This method has been shown to outperform traditional methods such as multi-atlas segmentation (Parvathaneni et al., 2019). This method also avoids slow-running inter-subject registration using geometric features using traditional parcellation methods (Fischl, 2012). Rather, it uses intermediate deformation fields to smoothly morph the geometric features and parcellation maps, generating full cortical parcellations in less than a minute.

2.3 | Feature extraction

In our experiments, we investigated three cortical shape features: cortical thickness, sulcal depth, and local gyrification. Cortical thickness [CT] is the width of the cortical gray matter and is computed using FreeSurfer (Fischl, 2012; Fischl & Dale, 2000). For sulcal depth and local gyrification index, the cerebral hull surface is used as the reference; the cerebral hull is the outer contour of the cortex and the pial surface is the inner contour (see Figure 1; Lyu, Kim, Girault, et al., 2018; Moorhead et al., 2006). Sulcal depth [SD] is the geodesic distance between the pial surface and the cerebral hull (Lyu, Kang, Woodward, & Landman, 2018). Gyrification index is defined as the area ratio between the cerebral hull and the pial surface and local gyrification index [LGI] is the local ratio computed by a shape-adaptive kernel for a sulcal point on the inner contour (Lyu, Kim, Girault, et al., 2018). Figure 1 (top panel) visualizes the CT, SD, and LGI measurements on the cortex.

After the above surface reconstruction pipeline, sulcal and gyral regions were segmented (Lyu, Kim, Woodward, et al., 2018). From these, an adaptive kernel traversed cortical regions at a spatially varying diffusion speed along sulci and gyri to compute the pial/hull area ratio (Lyu, Kim, Girault, et al., 2018). After feature extraction, 1110 sets of feature maps, such as those shown in Figure 1 (bottom panel), were visually quality controlled to identify anomalous or unusable results. 25 sets were excluded from the study as they failed visual inspection at various stages of preprocessing. We excluded two additional subjects from the dataset because they were missing classification as a control or patient. This led to a final cohort of 1083 sets of feature maps included in our study.

Via regression, we verified that sulcal depth is correlated with total intra-cranial volume [TICV], generating hard-to-interpret results. To compensate, sulcal depth values for each session were divided by the cubic root of the TICV of the subject associated with that session. Division by the TICV cubic root reduced multicollinearity (Multicollinearity, 2010) among sulcal depth measurements, stabilizing the detected differences. For the purpose of this normalization, TICV was computed as the volume of the FreeSurfer segmentation map.

2.4 | Statistical analysis

The longitudinal structure of the data was handled using a linear mixed model [LMM], through which we compared the diagnostic groups differences from study entry (intercept) changing over time (slope) with the control intercepts (Long et al., 2018). Suppose that Y_{ij} is the imaging measure for the ith participant $(i = 1, \ldots, N)$ at the jth visit $(j = 1, \ldots, n_i)$, where n_i is the number of visits of the ith participant. The LMM for the analysis was:

$$Y_{ij} = \beta_0 t_{ij} + \beta_1 a_{ij} + \beta_2 s_i + \beta_3 g_{0i} + \beta_4 g_{1i} + \beta_5 g_{2i} + \beta_6 g_{3i} + b_i + \epsilon_{ij} \quad (1)$$

where β_k is a fixed effect; t_{ij} is the duration computed as the age at the current (jth) scan minus the age at the first scan; a_{ij} is the subject's age at the current scan; s_i encodes sex (0 = female, 1 = male); $g_{0i}, g_{1i}, g_{2i}, g_{3i}$ encodes membership in each of the control, CAP_{low}, CAP_{med}, and CAP_{high} groups (0 = not in class, 1 = in class) at study entry, respectively; b_i is a random effect encoding session belonging to each subject and assumed to be normally distributed; and ϵ_{ij} is the residual which accounts for effects that are otherwise unexplained by the other variables and is assumed to be normally distributed and orthogonal to b_i. Under the normality assumption, estimation is carried out using maximum likelihood methods (Verbeke & Molenberghs, 2000). The objects of inference in the model of Equation (1) are the group intercepts $\beta_3, \beta_4, \beta_5, \beta_6$ and, more specifically, the differences between the control intercept and the CAP group intercepts (e.g., $\beta_3 - \beta_4$). The group mean was not used. An omnibus null hypothesis of no difference between any of the CAP groups and controls was evaluated using a Wald-type test statistic.

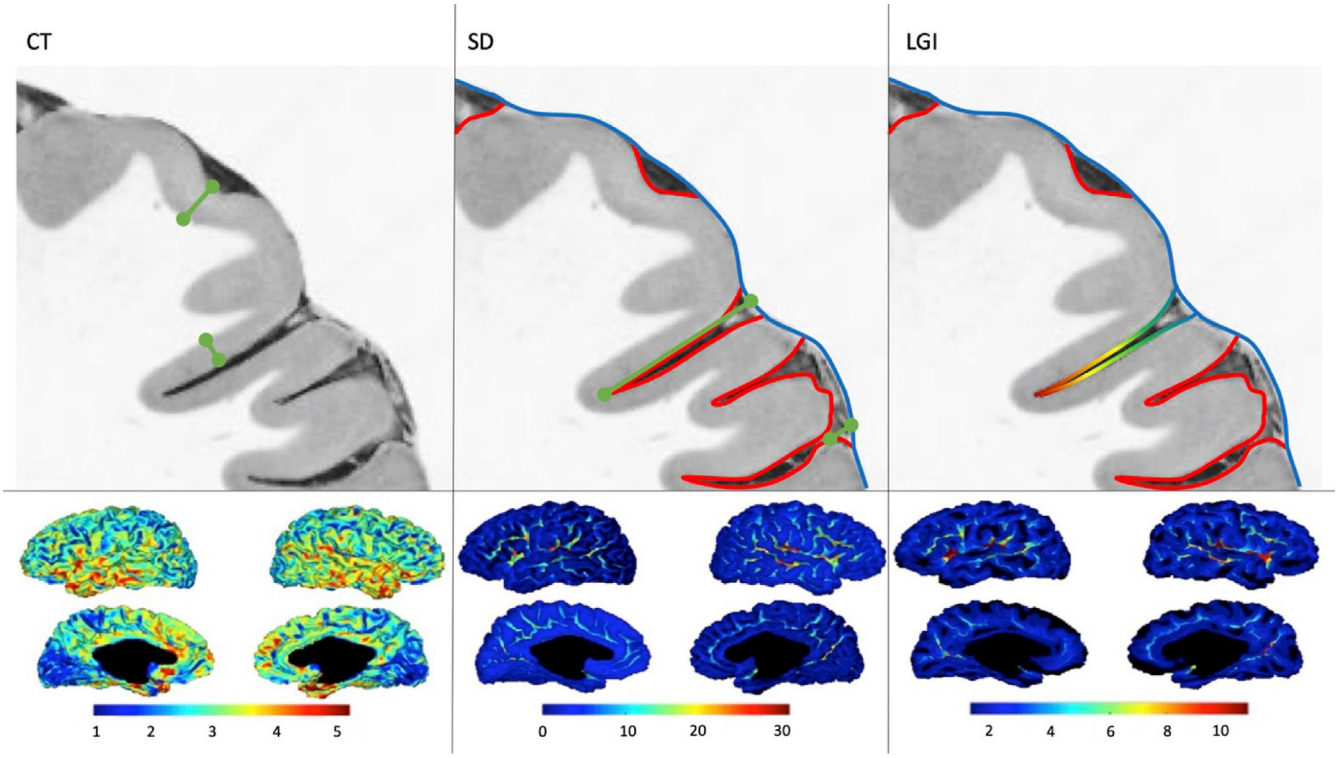

FIGURE 1 Cortical measurement visualizations on an example cortical section (top) and examples of the full feature maps (bottom). For CT and SD, the green bars indicate the measured geodesic distance between vertices. For SD and LGI, the red contour indicates the pial surface and the blue contour indicates the cerebral hull. LGI is then defined as the ratio of the (red surface area)/(blue surface area), using a shape-adaptive local kernel. The gradients for LGI and the bottom figures signify where magnitude is expected to be greater (red) and lesser (blue). The grey and white matter surface originates from Reference Roberts et al. (1970).

p values were adjusted for multiple comparisons with a family-wise error rate [FWER] correction based on random field theory (Taylor & Worsley, 2007; Worsley et al., 1999). Multi-comparison correction was not considered between features as they are treated separately and never directly statistically compared.

Note that each session can only belong to one group, that is, only one of $g_{0ij}, g_{1ij}, g_{2ij}, g_{3ij}$ equals 1 while the rest equal 0. Therefore, group intercept values ($\beta_3 \ldots \beta_6$)are used to compare the model fits for each group in different brain areas. The sampling distributions for these values can illuminate trends corresponding to disease progression.

2.5 | Implementation details

Linear mixed models were fitted using the lme4 package in R (Bates et al., 2015), which is a general linear model toolbox. SurfStat (Worsley et al., 2009), which is a MATLAB toolbox for linear mixed effects models and random field theory on brain surface and volumetric data, was used for surface smoothing, multiple comparison correction, and displaying results. To denoise the CT input, we applied a Gaussian smoothing kernel (full width at half maximum [FWHM] = 6 mm) using SurfStat, which provides the best balance between conservative analysis and preserving sensitivity (Han et al., 2006).

2.6 | Data availability statement

The data that support the findings of this study are available on request from the corresponding author. The data are not publicly available due to restrictions, for example, their containing information that could compromise the privacy of research participants. The code for our statistical analysis is available at https://github.com/MedICL-VU/Cortical-Shape-Analysis-in-HD.

3 | RESULTS

3.1 | Cortical thickness

Figure 2 shows the brain map of regions showing statistically significant CT differences based on the omnibus testing (top panel), and boxplots of the associated group intercept estimates (bottom panel). CT appears highly sensitive to changes in the primary motor cortex, with a high occurrence of statistically significant changes on the precentral gyrus (Figure 2, top panel). CT is the only feature that captures differences with higher *p* values ($p < 0.05$), shown in darker shades of blue. CT alterations were mostly detected in the posterior regions while very few significant changes appeared in the anterior regions. Group intercepts fit similarly in analogous regions in both

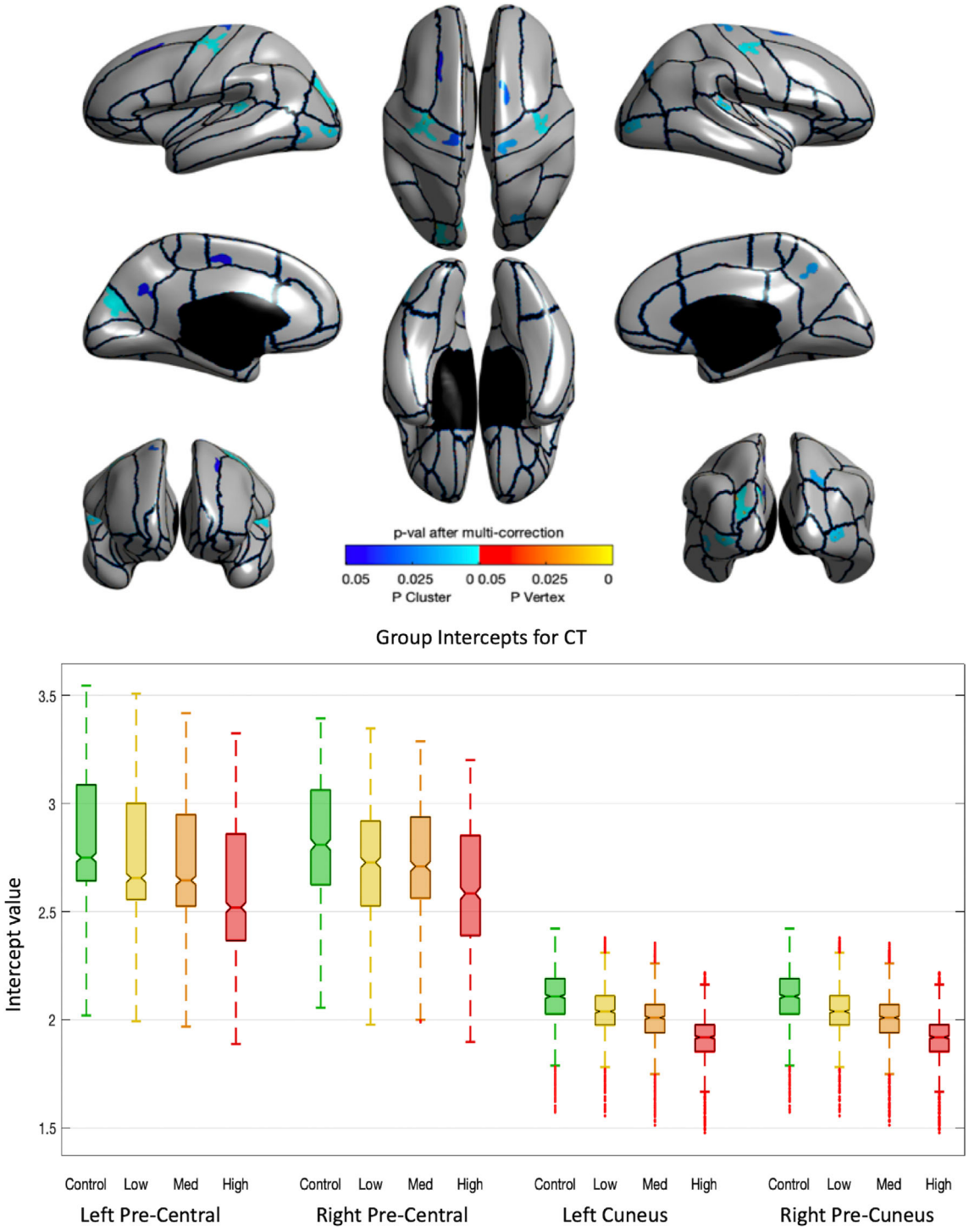

FIGURE 2 Omnibus test results (top) and cluster intercept boxplots (bottom) for CT. *p* values were adjusted for FWER using random field theory $(\alpha = 0.01)$.

hemispheres and marked an inverse relationship between the mean intercept value in the region and the level of disease progression (Figure 2, bottom panel). Note that only CT exhibits outliers in these figures.

Figure 3 shows CT effect size (left) and T-test results (right) using a stratified analysis of the difference between controls and each of the CAP_{low} (top), CAP_{med} (middle), and CAP_{high} (bottom) groups. CT displays an increase in effect size with disease progression, across the entire cortical surface. The regions with statistically significant differences for CT are: pre-central, pre-cuneus, cuneus, superior temporal, superior frontal, inferior parietal, superior parietal, and lateral occipital. The *p* values and group mean intercepts for these regions are provided in Table S1. Figure S1 shows the effect of age on the CT measurements after smoothing and after fitting the model.

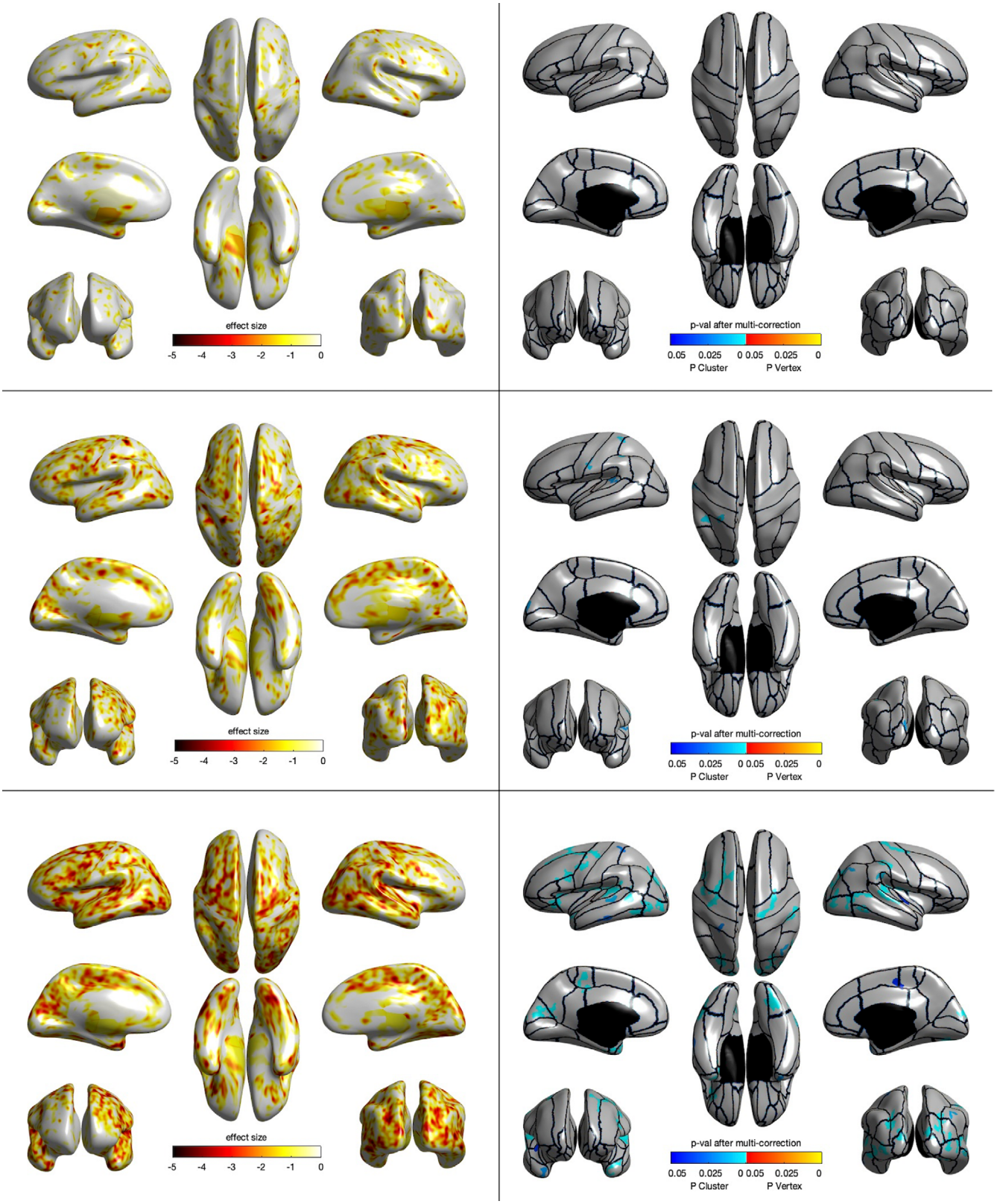

FIGURE 3 Effect size (left) and T-test results (right) for the difference between controls and CAP_{low} (top), CAP_{med} (middle), and CAP_{high} (bottom) for CT. The T-test comparison for each stratum is $\beta_3 - \beta_j$ where j corresponds to the intercept for each CAP group. Effect size is computed by SurfStat using Cohen's coefficient

3.2 | Sulcal depth

Among the three investigated features, SD showed the fewest significant differences and upon observation also the smallest clusters on average (Figure 4, top panel). However, SD indicates the same decreasing trend between intercept value and disease progression as CT (Figure 4, bottom panel).

Figure 5 shows SD effect size (left) and *T*-test results (right) for the difference between controls and CAP_{low} (top), CAP_{med} (middle), and CAP_{high} (bottom). SD effect sizes increase with disease

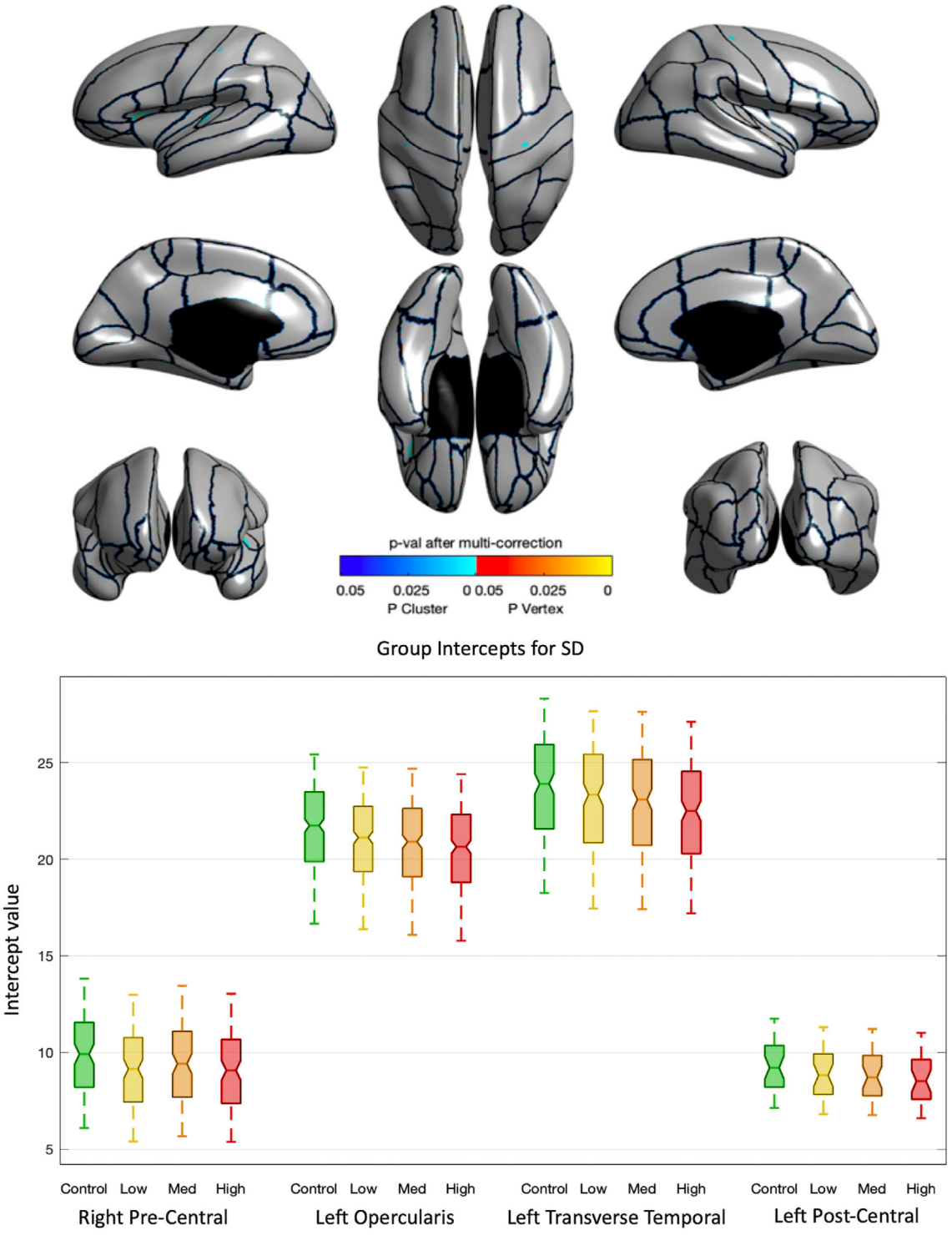

FIGURE 4 Omnibus test results (top) and cluster intercept boxplots (bottom) for SD. *p* values were adjusted for FWER using random field theory ($\alpha = 0.01$).

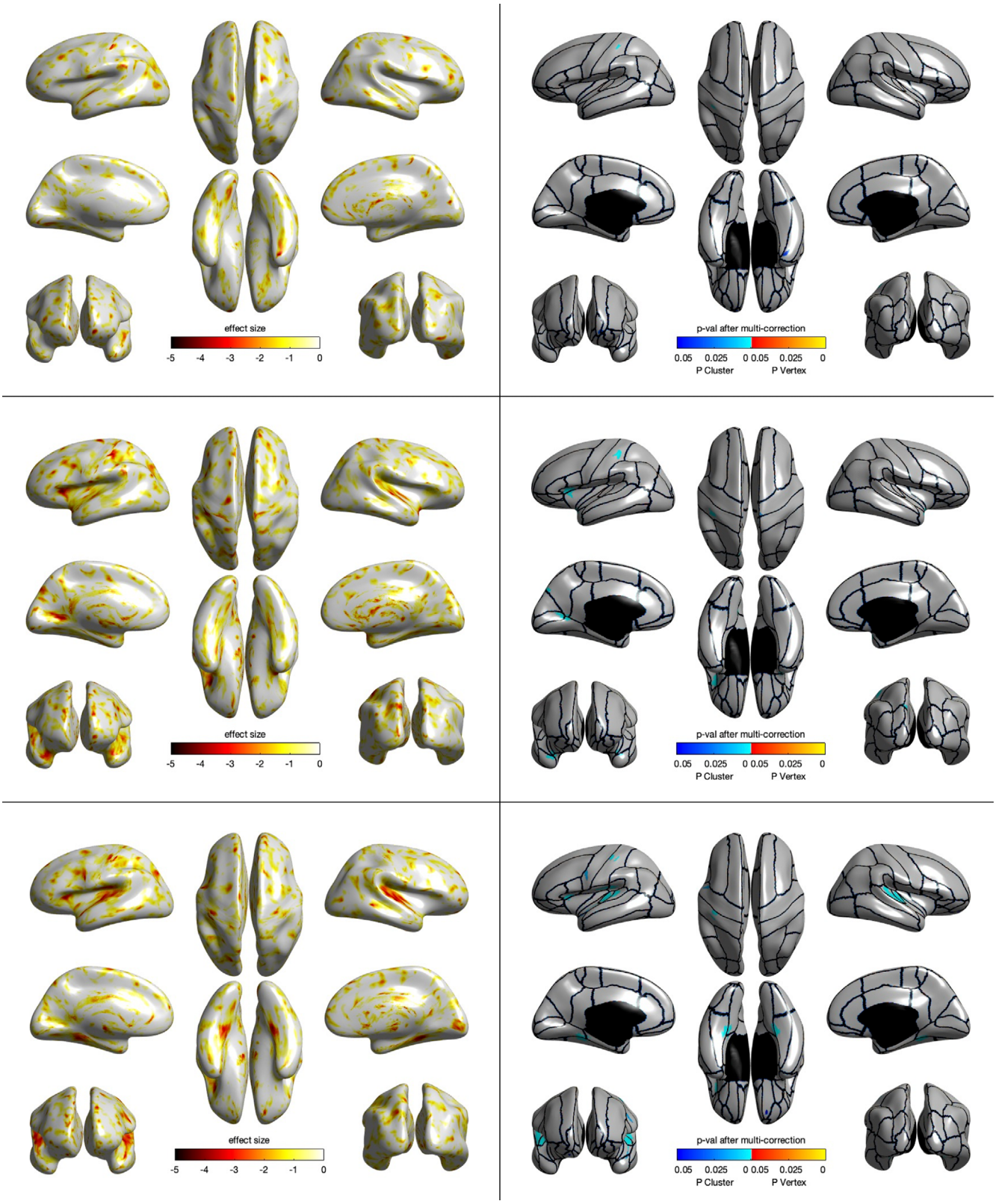

FIGURE 5 Effect size (left) and *T*-test results (right) for the difference between controls and CAP_{low} (top), CAP_{med} (middle), and CAP_{high} (bottom) for SD. The *T*-test comparison for each stratum is $\beta_3 - \beta_j$ where *j* corresponds to the intercept for each CAP group. Effect size is computed by SurfStat using Cohen's coefficient

progression with noteworthy effects in the left opercularis and the insula. The regions with detected differences for SD are: pre-central, post-central, transverse temporal, and opercularis. The *p* values and group mean intercepts are provided in Table S2. Figure S2 shows the effect of age on the SD measurements after fitting the model.

3.3 | Local gyrification index

Group differences based on LGI appears uniquely significant in the insular regions (Figure 6, top panel), which may correlate with changes in the basal structures. Like CT, LGI detects differences on the pre-

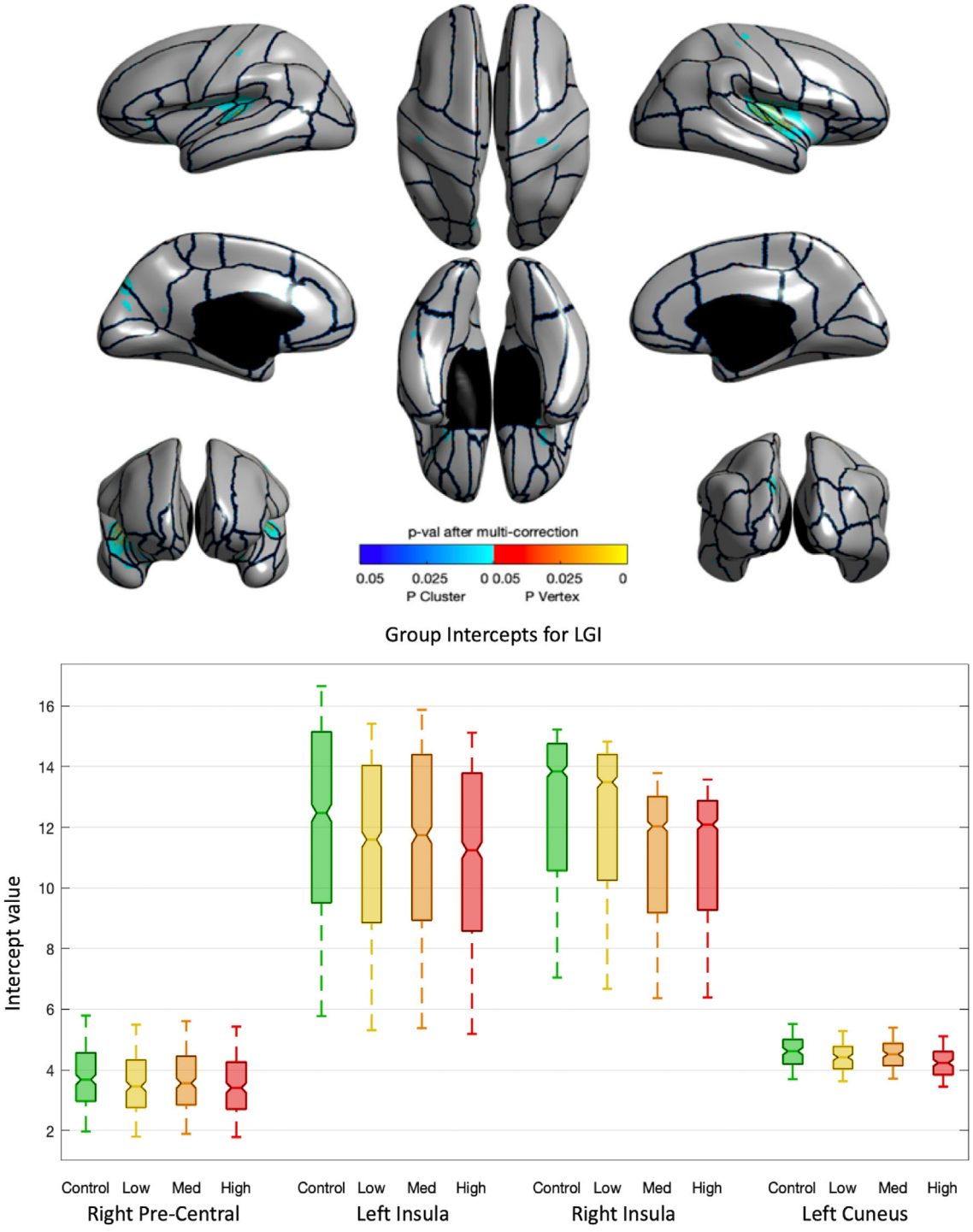

FIGURE 6 Omnibus test results (top) and cluster intercept boxplots (bottom) for LGI. *p* values were adjusted for FWER using random field theory ($\alpha = 0.01$).

central gyrus and in the posterior regions. LGI stands apart from the other two cortical shape features in that it detects clusters of insular changes in both hemispheres, although more pronounced in the right hemisphere. The insular clusters for LGI also show a high concentration of significant peaks which corresponds to many detected clusters cooccurring in these regions. LGI also demonstrates the same decreasing intercept pattern as CT and SD (Figure 6, bottom panel).

Figure 7 shows LGI effect size (left) and *T*-test results (right) for the difference between controls and CAP_{low} (top), CAP_{med} (middle), and CAP_{high} (bottom). LGI displays a large effect in the insula with distinctly increasing effect as the disease progresses. Small pockets of greater effect size beyond the insula coincide with areas of significant change, as well as some that do not. The regions with detected differences for LGI are: pre-central, post-central, pre-cuneus, cuneus, insular, transverse temporal, superior temporal, inferior temporal, and supra-marginal. The *p* values and group mean intercepts are summarized in Table S3. Figure S3 shows the effect of age on the LGI measurements after fitting the model.

4 | DISCUSSION

4.1 | Feature comparison

4.1.1 | Cortical thickness

The results indicate that pre-central and post-central gyri around the central sulcus, which correspond to the primary motor and somatosensory cortices, are highly affected. Previous studies suggest that cortical thinning progresses posteriorly to anteriorly and affects the sensorimotor region most (Rosas et al., 2002). Consistent with this conceptualization of cortical thinning progression in Huntington's disease, our results show differences in cortical thickness at the posterior poles more than the anterior poles and conspicuously show that the most statistically affected region is the sensorimotor area. Effect sizes for CT display an increasing trend correlated to disease progression. However, areas of effect for CT are ubiquitous across the cortical surface. These findings suggest that CT correlates with Huntington's disease-related changes but does not uniquely correlate with specific areas that could conclusively indicate the presence of disease, suggesting that most of its detected areas of change could have practical utility.

4.1.2 | Sulcal depth

In our analysis, regional changes for SD are largely inconclusive in most brain regions, which suggests that SD measures are generally less sensitive to anatomical changes during the course of Huntington's disease compared with the other two features. Only two areas in the pre-central and transverse temporal regions show significant cortical differences between control and Huntington's disease patients, which may suggest changes in the primary motor and auditory cortices, respectively. Hence, these detections parallel known pathology as well as findings from the other two features. It is noteworthy that SD captured differences in the left opercularis, which was an area largely undetected by the other features. SD effect sizes increase with disease progression; the left opercularis has a large effect size suggesting this detection may have practical significance.

4.1.3 | Local gyrification index

The insular changes that LGI identified are of particular importance since this area was largely ignored by cortical thickness measures in prior studies (Nopoulos et al., 2010; Rosas et al., 2002; Tabrizi et al., 2013). Since insular differences correspond to the basal ganglia where the putamen and caudate nucleus are preferentially affected in pre-symptomatic Huntington's disease (Hennenlotter et al., 2004), LGI may promise some degree of early detection. Despite LGI overtly detecting in the insula, it also has a posterior–anterior association similar to CT, with a few clusters near the cuneus and virtually no clusters detected anteriorly. However, unlike CT and SD, LGI results strongly detected in the insula in both T-testing and omnibus testing, at every acceptance threshold with which we experimented, with and without multi-comparison correction. LGI displays large effect sizes mainly in the insula with a few other small areas scattered along the cortical surface. Like CT and SD, LGI's effect size is distinctly correlated with disease progression. CAP_{high} shows the strongest effect in the insula in both hemispheres, yet CAP_{med} also shows a strong effect in the insular areas particularly in the left hemisphere, indicating that LGI could be a useful diagnostic tool for the reasons that CT is not.

Other neuroimaging research on PREDICT-HD suggests that markers create patterns that may allow detection decades prior to clinical diagnosis (Paulsen et al., 2008). However, to discover such patterns, we need evidence of where features might be changing in the cortex. The strength of the evidence that a feature is changing within a given anatomical structure can be quantified by the total number of detected vertices relative to the total number of vertices of the structure. Table 2 outlines the global and regional surface areas for each feature in structures where that feature changed.

4.2 | Regional analysis

In addition to a global cortex analysis, we also compared the average of group intercepts for select regions (Figures 2, 4, and 6, bottom panels). The consistent stepwise decrease in average intercept values reflects neurodegeneration caused by Huntington's disease since the magnitude of these metrics should generally decrease with disease progression (Nopoulos et al., 2010; Rosas et al., 2002). The similarity in the intercept values for detected changes within the same regions on separate hemispheres suggests that regional model fits are preserved across the features and throughout the corresponding structure for controls and diagnostic groups. High intercept values for LGI in the insula indicate high correlation for changes in LGI in these

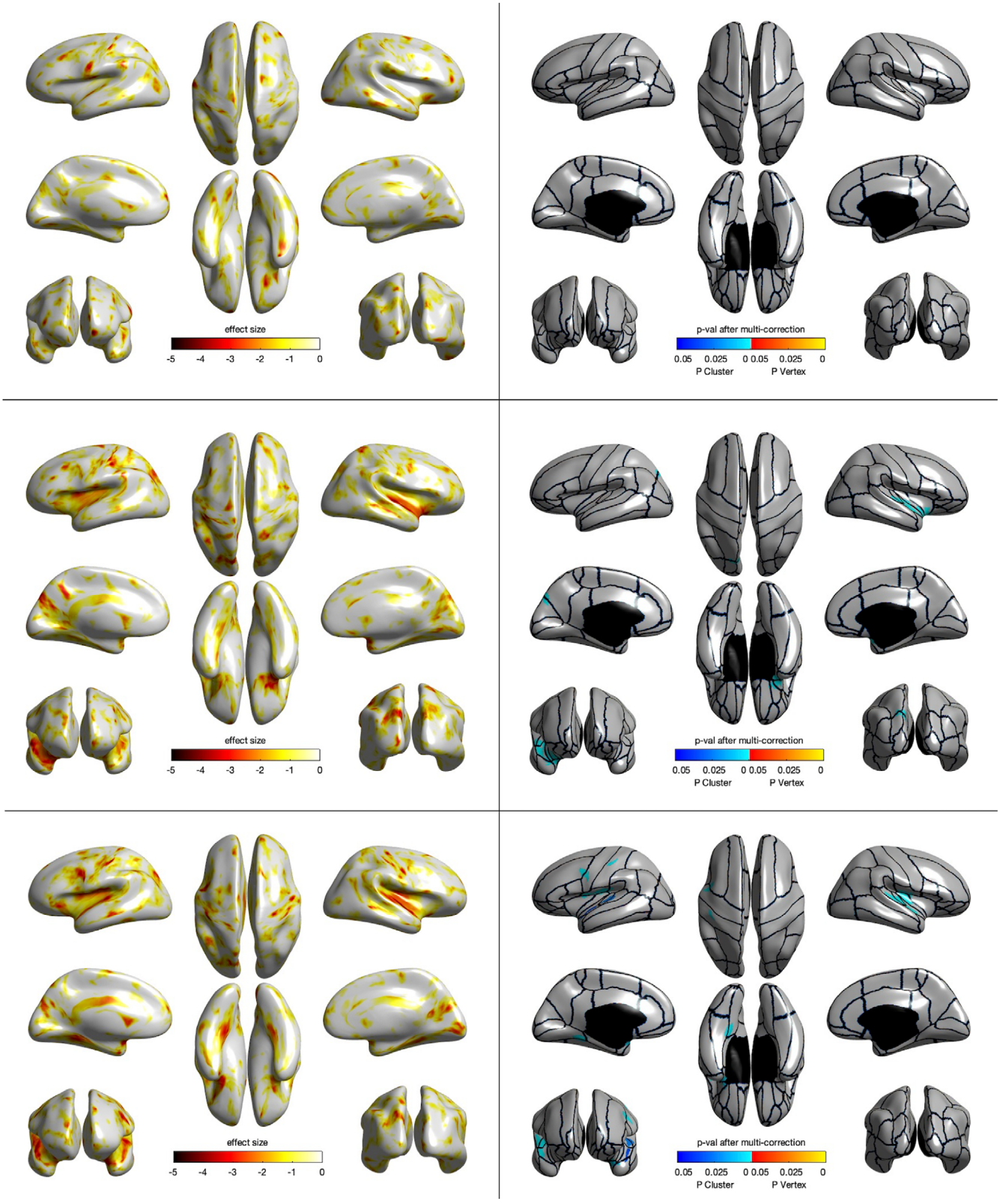

FIGURE 7 Effect size (left) and T-test results (right) for the difference between controls and CAP_{low} (top), CAP_{med} (middle), and CAP_{high} (bottom) for LGI. The *T*-test comparison for each stratum is $\beta_3 - \beta_j$ where j corresponds to the intercept for each CAP group. Effect size is computed by SurfStat using Cohen's coefficient

TABLE 2 Summary of regions with significant changes per feature

	Cortical thickness		Sulcal depth		Local gyrification index	
	Left	Right	Left	Right	Left	Right
Precentral gyrus[a]	17.45	13.24	–	1.27	–	2.76
Precuneus[a]	3.77	4.84	0.60	–	4.12	–
Cuneus[b]	32.38	–	–	–	12.13	–
Postcentral gyrus[b]	–	–	0.32	–	1.16	0.65
Planum temporal[b]	30.93	30.97	–	–	15.37	8.33
Sup. Occ. Gyrus[b]	43.57	–	–	–	2.36	–
Trans. Temp. Gyrus[b]	–	–	13.96	–	80.02	–
Anterior insula	–	–	–	–	3.98	38.94
Central operculum	–	–	–	–	39.97	48.39
Entorhinal area	–	–	–	–	–	10.17
Frontal operculum	–	–	21.95	–	–	–
Fusiform gyrus	–	–	0.64	0.74	–	–
Inf. Occ. gyrus	21.03	12.07	–	–	–	–
Inf. Temp. gyrus	–	–	–	–	1.12	–
Orb. Inf. frontal gyrus	–	–	–	–	10.29	–
Post. insula	–	–	–	–	22.57	68.82
Parietal operculum	–	–	–	–	38.70	20.16
Post. Orb. gyrus	–	–	–	–	7.25	8.71
Planum polare	–	–	–	–	–	68.46
Sup. frontal gyrus	3.42	3.35	–	–	–	–
Suppl. motor cortex	8.85	–	–	–	–	–
Sup. parietal lobe	–	6.00	–	–	–	–
Temp. pole	–	–	–	–	–	5.45
Trans. temp. gyrus	–	–	–	–	–	84.44

Note: The percentage of the structure with significant changes are reported, in terms of the number of vertices. The parcellation scheme is used to identify regional belonging and compute the percentage of detected vertices within the region. Regions are sorted according to cooccurrence in the three features. Otherwise, regional changes were detected by only one of the features. –, no feature changes detected for the region in the corresponding hemisphere.

[a]Regional changes were detected by all three features.

[b]Regional changes were detected by two of the features.

regions, which would further support LGI as a potential early biomarker.

The somatic expansion theory suggests that neurodevelopment is normal until expansion reaches a threshold in midlife (Hong et al., 2021; Mangin et al., 2020). In support, neurodevelopmental changes do not appear to account for the detected changes as the changes in CAP_{low} group is not significantly different from controls (Figures 3, 5, and 7, top panels; Scahill et al., 2020). This strongly suggests that neurodegeneration, rather than neurodevelopmental defect, is responsible for the differences identified in our study; however, definitive confirmation of this would necessitate scanning subjects over their entire lifespan.

Shown in Figure S4, we additionally observe that our model can correlate clusters that span multiple structures, such as a cluster that overlaps with both the cuneus and pre-cuneus. We note that these detections are undeterred by differences in cortical shape that delineate different cortical structures, and the relative intercept values alter accordingly. Thus, cluster outliers may appear on the cluster fringes that overlap with other regions where the model attempts to fit intercepts that deviate from the majority of the cluster.

4.3 | Comparison with previous literature

Prior studies have examined cortical morphology in Huntington's disease and reported that cortical thinning occurs most prominently in the posterior and superior cerebral cortex (Nopoulos et al., 2010; Rosas et al., 2002) and occurs variably between patients and between diagnostic groups (Rosas et al., 2002). Our findings for CT are consistent with these prior findings, with a higher relative concentration of posterior changes compared with anterior changes and the appearance of most clusters in the superior cerebral regions, for example,

the sensorimotor area. CT did not detect any superfluous differences that were not already discovered in prior Huntington's disease studies using CT. Instead of solely focusing on one feature, our paper adds a comprehensive analysis comparing changes between CT, SD, and LGI to the literature, which yields better contextual understanding of CT as an indicator for Huntington's disease.

A prior study on SD in Huntington's disease identified a global decrease in sulcal depth in Huntington's disease(Nopoulos et al., 2012) and another found a localized decrease in sulcal depth in the Sylvian fissure (Mangin et al., 2020). Global decrease suggests that SD is not a precise tool for detecting Huntington's disease-related cortical changes, which our findings for SD support yielding few significant differences from controls. Additionally, one of those differences was detected in the transverse temporal gyrus, which is located on the Sylvian fissure (Brown, 2005), aligning our findings with prior study.

Prior studies using LGI in the context of other diseases found that this novel measure yields higher reproducibility than conventional methods and captures both positive and negative changes in gyrification (Lyu, Kim, Girault, et al., 2018). To our knowledge, no previous literature on Huntington's disease applies LGI suggesting that our study is the premier for this feature in the context of Huntington's disease, and our findings are therefore novel.

4.4 | Clinical interpretation

Our results show that both CT and LGI correlate with changes due to Huntington's disease in many cortical regions; CT and LGI capture 9 and 18 different regions of change, respectively. Additionally, CT and LGI also correlate with specific regions of interest. We note that, the consistency of insular detection for LGI potentially implies greater reliability compared with CT in detecting Huntington's disease-related cortical changes. Nonetheless, the detected areas for LGI and CT appear complementary to each other, focusing on different areas affected by neurodegeneration. Together, the two could better characterize patient neurodegeneration and have even greater sensitivity and reliability than if one were singularly used, which may ultimately contribute to prediction and early detection. The complementarity of the two features regarding clinical prediction outcomes will be investigated in future work.

5 | CONCLUSION

Validating potential markers of Huntington's disease is a critical step in asserting the reliability of early detection measures. In this study, we propose an analysis of cortical changes using three different features: cortical thickness, sulcal depth, and local gyrification index. Our results reveal local gyrification index as a potentially eminent marker for early detection with strong correlation to regional differences not captured by cortical thickness. Local gyrification index and cortical thickness were comparable overall with similar patterns in their collocated detections. However, local gyrification index detected differences in regions previously undetected by cortical thickness in prior studies. Future direction for this research will involve correlations between cortical morphology and the motor, cognitive and behavioral scores provided by PREDICT-HD.

ACKNOWLEDGMENTS

These Huntington's disease studies would not be possible without the vital contribution of the research participants and their families. Individuals who contributed to the collection subject data can be found at https://www.enroll-hd.org/enrollhd_documents/2018-10-R1/Enroll-HD-Acknowledgement-List-Public-2018-10-R1.pdf, in the Supplementary Material of Lee et al. (https://doi.org/10.1093/hmg/ddx286), and in the Supplemental Information of Genetic Modifiers of Huntington's Disease (GeM-HD) Consortium (https://doi.org/10.1016/j.cell.2015.07.003). Supported by the CHDI Foundation (U.S.), the U.S. National Institutes of Health (NS082079, NS091161, NS016367, NS049206, NS105709, NS114065, NS119471, NS040068), the Medical Research Council (UK; MR/L010305/1 and fellowship MR/P001629/1), and a Cardiff University School of Medicine studentship.

FUNDING INFORMATION

This study was supported, in part, by the NIH grant R01—NS094456 and National Research Foundation of Korea (NRF) grant 2021R1G1A1094359. The PREDICT-HD study was funded by the NCATS, the NIH (NIH; R01—NS040068, U01—NS105509, U01—NS103475) and CHDI.org. Vanderbilt University Institutional Review Board has approved this study.

CONFLICT OF INTEREST

The authors declare no conflict of interest.

ORCID

Zachary A. Stoebner https://orcid.org/0000-0001-6947-6638
Kilian Hett https://orcid.org/0000-0001-8831-4247

REFERENCES

Bates, D., Mächler, M., Bolker, B. M., & Walker, S. C. (2015). Fitting linear mixed-effects models using lme4. *Journal of Statistical Software*, *67*(1), 1–48. https://doi.org/10.18637/jss.v067.i01

Brown, K. (2005). *Encyclopedia of language and linguistics* (Vol. 1). Elsevier.

Ehrlich, M. E. (2012). Huntington's disease and the striatal medium spiny neuron: Cell-autonomous and non-cell-autonomous mechanisms of disease. *Neurotherapeutics*, *9*(2), 270–284. https://doi.org/10.1007/s13311-012-0112-2

Fischl, B. (2012). FreeSurfer. *Neuroimage.*, *62*(2), 774–781. https://doi.org/10.1016/j.neuroimage.2012.01.021.FreeSurfer

Fischl, B., & Dale, A. M. (2000). Measuring the thickness of the human cerebral cortex from magnetic resonance images. *Proceedings of the National Academy of Sciences of the United States of America*, *97*(20), 11050–11055. https://doi.org/10.1073/pnas.200033797

Han, X., Jovicich, J., Salat, D., van der Kouwe, A., Quinn, B., Czanner, S., Busa, E., Pacheco, J., Albert, M., Killiany, R., Maguire, P., Rosas, D., Makris, N., Dale, A., Dickerson, B., & Fischl, B. (2006). Reliability of MRI-derived measurements of human cerebral cortical thickness: The

effects of field strength, scanner upgrade and manufacturer. *NeuroImage*, *32*(1), 180–194. https://doi.org/10.1016/j.neuroimage.2006.02.051

Hedreen, J. C., Peyser, C. E., Folstein, S. E., & Ross, C. A. (1991). Neuronal loss in layers V and VI of cerebral cortex in Huntington's disease. *Neuroscience Letters*, *133*(2), 257–261. https://doi.org/10.1016/0304-3940(91)90583-F

Hennenlotter, A., Schroeder, U., Erhard, P., Haslinger, B., Stahl, R., Weindl, A., von Einsiedel, H., Lange, K. W., & Ceballos-Baumann, A. O. (2004). Neural correlates associated with impaired disgust processing in pre-symptomatic Huntington's disease. *Brain*, *127*(6), 1446–1453. https://doi.org/10.1093/brain/awh165

Hett, K., Johnson, H., Coupe, P., Paulsen, J. S., Long, J. D., & Oguz, I. (2020). Tensor-based grading: A novel patch-based grading approach for the analysis of deformation fields in Huntington's disease. *IEEE 17th International Symposium on Biomedical Imaging*, 1091–1095. https://doi.org/10.1109/ISBI45749.2020.9098692

Hong, E. P., MacDonald, M. E., Wheeler, V. C., et al. (2021). Huntington's disease pathogenesis: Two sequential components. *J Huntingtons Dis.*, *10*(1), 35–51. https://doi.org/10.3233/JHD-200427

Hong, Y., O'Donnell, L. J., Savadjiev, P., et al. (2018). Genetic load determines atrophy in hand cortico-striatal pathways in presymptomatic Huntington's disease. *Human Brain Mapping*, *39*(10), 3871–3883. https://doi.org/10.1002/hbm.24217

Klein, A., Canton, T. D., Ghosh, S. S., et al. (2010). Open labels: Online feedback for a public resource of manually labeled brain images. 16th Annual Meeting of the Organization for Human Brain Mapping. Published online 2010: 84358.

Li, H., Zhang, H., Hu, D., Johnson, H., Long, J. D., Paulsen, J. S., & Oguz, I. (2020). Generalizing MRI subcortical segmentation to neurodegeneration. In *MLCN workshop*, *MICCAI* (pp. 139–147). Springer. https://doi.org/10.1007/978-3-030-66843-3_14

Li, H., Zhang, H., Johnson, H., Long, J., Paulsen, J., & Oguz, I. (2021a). Longitudinal subcortical segmentation with deep learning. In: SPIE Medical Imaging 2021: Image processing. *International Society for Optics and Photonics*, 11596. https://doi.org/10.1117/12.2582340

Li, H., Zhang, H., Johnson, H., Long, J., Paulsen, J., & Oguz, I. (2021b). MRI subcortical segmentation In neurodegeneration with cascaded 3D CNNs. In: SPIE Medical Imaging: Image processing. *International Society for Optics and Photonics*, 11596. https://doi.org/10.1117/12.2582005

Long, J. D., Lee, J. M., Aylward, E. H., Gillis, T., Mysore, J. S., Abu Elneel, K., Chao, M. J., Paulsen, J. S., MacDonald, M. E., & Gusella, J. F. (2018). Genetic modification of Huntington disease acts early in the Prediagnosis phase. *American Journal of Human Genetics*, *103*(3), 349–357. https://doi.org/10.1016/j.ajhg.2018.07.017

Lyu, I., Kang, H., Woodward, N. D., & Landman, B. A. (2018). Sulcal depth-based cortical shape analysis in normal healthy control and schizophrenia groups. *Proc SPIE Int Soc Opt Eng*, 10574. https://doi.org/10.1117/12.2293275

Lyu, I., Kang, H., Woodward, N. D., Styner, M. A., & Landman, B. A. (2019). Hierarchical spherical deformation for cortical surface registration. *Medical Image Analysis*, *57*, 72–88. https://doi.org/10.1016/j.media.2019.06.013

Lyu, I., Kim, S. H., Girault, J. B., Gilmore, J. H., & Styner, M. A. (2018). A cortical shape-adaptive approach to local gyrification index. *Medical Image Analysis*, *48*, 244–258. https://doi.org/10.1016/j.media.2018.06.009

Lyu, I., Kim, S. H., Woodward, N. D., Styner, M. A., & Landman, B. A. (2018). TRACE: A topological graph representation for automatic sulcal curve extraction. *IEEE Transactions on Medical Imaging*, *37*(7), 1653–1663. https://doi.org/10.1109/TMI.2017.2787589

Mangin, J. F., Rivière, D., Duchesnay, E., Cointepas, Y., Gaura, V., Verny, C., Damier, P., Krystkowiak, P., Bachoud-Lévi, A. C., Hantraye, P., Remy, P., & Douaud, G. (2020). Neocortical morphometry in Huntington's disease: Indication of the coexistence of abnormal neurodevelopmental and neurodegenerative processes. *NeuroImage Clin.*, *26*, 102211. https://doi.org/10.1016/j.nicl.2020.102211

Moorhead, T. W. J., Harris, J. M., Stanfield, A. C., Job, D. E., Best, J. J. K., Johnstone, E. C., & Lawrie, S. M. (2006). Automated computation of the Gyrification index in prefrontal lobes: Methods and comparison with manual implementation. *NeuroImage*, *31*(4), 1560–1566. https://doi.org/10.1016/j.neuroimage.2006.02.025

Multicollinearity, A. A. (2010). Wiley Interdiscip rev. *Computational Statistics*, *2*(3), 370–374. https://doi.org/10.1002/wics.84

Nopoulos, P., Magnotta, V. A., Ph, D., et al. (2012). Morphology of the cerebral cortex in preclinical Huntington's disease. *The American Journal of Psychiatry*, *164*, 1428–1434.

Nopoulos, P. C., Aylward, E. H., Ross, C. A., Johnson, H. J., Magnotta, V. A., Juhl, A. R., Pierson, R. K., Mills, J., Langbehn, D. R., Paulsen, J. S., & PREDICT-HD Investigators Coordinators of Huntington Study Group (HSG). (2010). Cerebral cortex structure in prodromal Huntington disease. *Neurobiology of Disease*, *40*(3), 544–554. https://doi.org/10.1016/j.nbd.2010.07.014

Parvathaneni, P., Bao, S., Nath, V., et al. (2019). Cortical surface parcellation using spherical convolutional neural networks. *Medical Image Computing and Computer Assisted Intervention – MICCAI 2019*. *MICCAI 2019*. *Lecture Notes in Computer Science*, 11766. Springer, Cham. https://doi.org/10.1007/978-3-030-32248-9_56

Paulsen, J. S., Langbehn, D. R., Stout, J. C., Aylward, E., Ross, C. A., Nance, M., Guttman, M., Johnson, S., MacDonald, M., Beglinger, L. J., Duff, K., Kayson, E., Biglan, K., Shoulson, I., Oakes, D., Hayden, M., & The Predict-HD Investigators and Coordinators of the Huntington Study Group. (2008). Detection of Huntington's disease decades before diagnosis: The Predict-HD study. *Journal of Neurology, Neurosurgery, and Psychiatry*, *79*(8), 874–880. https://doi.org/10.1136/jnnp.2007.128728

Paulsen, J. S., Nopoulos, P. C., Aylward, E., Ross, C. A., Johnson, H., Magnotta, V. A., Juhl, A., Pierson, R. K., Mills, J., Langbehn, D., Nance, M., & PREDICT-HD Investigators and Coordinators of the Huntington's Study Group (HSG). (2010). Striatal and white matter predictors of estimated diagnosis for Huntington disease. *Brain Research Bulletin*, *82*(3–4), 201–207. https://doi.org/10.1016/j.brainresbull.2010.04.003

Paulsen, J. S., Ph, D., Long, J. D., et al. (2015). Prediction of manifest Huntington disease with clinical and imaging measures: A 12-year prospective observational study. *Lancet Neurology*, *13*(12), 1193–1201. https://doi.org/10.1016/S1474-4422(14)70238-8.Prediction

Roberts, M., Hanaway, J., & Morest, D. K. (1970). *Atlas of the human brain in section* (2nd ed.). Lea & Febiger.

Rosas, H. D., Liu, A. K., Hersch, S., Glessner, M., Ferrante, R. J., Salat, D. H., van der Kouwe, A., Jenkins, B. G., Dale, A. M., & Fischl, B. (2002). Regional and progressive thinning of the cortical ribbon in Huntington's disease. *Neurology*, *58*(5), 695–701. https://doi.org/10.1212/WNL.58.5.695

Scahill, R. I., Zeun, P., Osborne-Crowley, K., Johnson, E. B., Gregory, S., Parker, C., Lowe, J., Nair, A., O'Callaghan, C., Langley, C., Papoutsi, M., McColgan, P., Estevez-Fraga, C., Fayer, K., Wellington, H., Rodrigues, F. B., Byrne, L. M., Heselgrave, A., Hyare, H., … Tabrizi, S. J. (2020). Biological and clinical characteristics of gene carriers far from predicted onset in the Huntington's disease young adult study (HD-YAS): A cross-sectional analysis. *Lancet Neurology*, *19*(6), 502–512. https://doi.org/10.1016/S1474-4422(20)30143-5

Tabrizi, S. J., Langbehn, D. R., Leavitt, B. R., et al. (2013). Biological and clinical manifestations of Huntington's disease in the longitudinal TRACK-HD study: cross-sectional analysis of baseline data. *Lancet Neurol*, *8*(9), 791–801. https://doi.org/10.1016/S1474-4422(09)70170-X.Biological

Tan X, Ross CA, Miller MI, Tang X. 2018. Changepoint analysis of putamen and thalamus subregions in premanifest Huntington's disease. In:

2018 IEEE 15th international symposium on biomedical imaging: 531–535. doi:https://doi.org/10.1109/ISBI.2018.8363632

Tang, X., Ross, C. A., Johnson, H., Paulsen, J. S., Younes, L., Albin, R. L., Ratnanather, J. T., & Miller, M. I. (2019). Regional subcortical shape analysis in premanifest Huntington's disease. *Human Brain Mapping*, *40*(5), 1419–1433. https://doi.org/10.1002/hbm.24456

Taylor, J. E., & Worsley, K. J. (2007). Detecting sparse signals in random fields, with an application to brain mapping. *Journal of the American Statistical Association*, *102*(479), 913–928. https://doi.org/10.1198/016214507000000815

Verbeke, G., & Molenberghs, G. (2000). *Linear mixed models for longitudinal data*. Springer. https://doi.org/10.1007/978-0-387-22775-7_3

Walker, F. O. (2007). Huntington's disease. *Lancet*, *369*(9557), 218–228. https://doi.org/10.1016/S0140-6736(07)60111-1

Worsley, K., Taylor, J., Carbonell, F., Chung, M. K., Duerden, E., Bernhardt, B., Lyttelton, O., Boucher, M., & Evans, A. C. (2009). SurfStat: A Matlab toolbox for the statistical analysis of univariate and multivariate surface and volumetric data using linear mixed effects models and random field theory. *NeuroImage*, *47*, S102. https://doi.org/10.1016/s1053-8119(09)70882-1

Worsley, K. J., Andermann, M., Koulis, T., MacDonald, D., & Evans, A. C. (1999). Detecting changes in nonisotropic images. *Human Brain Mapping*, *8*(2–3), 98–101. https://doi.org/10.1002/(SICI)1097-0193(1999)8:2/3<98::AID-HBM5>3.0.CO;2-F

Wu, D., Faria, A. V., Younes, L., Ross, C. A., Mori, S., & Miller, M. I. (2018). Whole-brain segmentation and change-point analysis of anatomical brain mri: Application in premanifest huntington's disease. *Journal of Visualized Experiments*, *2018*(136), 1–9. https://doi.org/10.3791/57256

Zhang, Y., Long, J. D., Mills, J. A., Warner, J. H., Lu, W., & Paulsen, J. S. (2011). Indexing disease progression at study entry with individuals at-risk for Huntington disease. *Am J Med Genet Part B Neuropsychiatr Genet.*, *156*(7), 751–763. https://doi.org/10.1002/ajmg.b.31232

SUPPORTING INFORMATION

Additional supporting information can be found online in the Supporting Information section at the end of this article.

How to cite this article: Stoebner, Z. A., Hett, K., Lyu, I., Johnson, H., Paulsen, J. S., Long, J. D., & Oguz, I. (2023). Comprehensive shape analysis of the cortex in Huntington's disease. *Human Brain Mapping*, *44*(4), 1417–1431. https://doi.org/10.1002/hbm.26125